Oxygen-Induced Transformations of an FeO(111) Film on Pt(111): A Combined DFT and STM Study

L. Giordano,*,† M. Lewandowski,‡ I. M. N. Groot,‡ Y.-N. Sun,‡ J. Goniakowski,§,∥ C. Noguera,§,∥ S. Shaikhutdinov,*,‡ G. Pacchioni,† and H.-J. Freund‡

Dipartimento di Scienza dei Materiali, Università di Milano-Bicocca, via Cozzi 53, 20125 Milano, Italy, Abteilung Chemische Physik, Fritz-Haber-Institut, Faradayweg 4-6, 14195 Berlin, Germany, and CNRS, Institut des Nanosciences de Paris, and UPMC Université Paris 06, INSP, UMR 7588, 4 place Jussieu, 75252 Paris cedex 05, France

The structural stability of an FeO(111) film supported on Pt(111) was studied by density functional theory (DFT) as a function of oxygen pressure. The results showed formation of O-rich phases at elevated O_2 pressures and revealed a site specificity of the oxidation process within the coincidence (Moiré) structure between FeO(111) and Pt(111), ultimately resulting in an ordered pattern of O−Fe−O trilayer islands, as observed by scanning tunneling microscopy (STM). In addition, high resolution STM images revealed a $(\sqrt{3} \times \sqrt{3})R30°$ superstructure of the FeO_2 islands with respect to pristine FeO(111). This structure is rationalized by DFT in terms of strong relaxations within the Fe sublayer and can be considered as an intermediate state of the FeO(111) transformation into an $Fe_2O_3(0001)$ film.

1. Introduction

Thin oxide films grown on metal substrates have attracted considerable attention for potential applications in microelectronics, magnetic devices, and catalysis.[1−6] Their peculiar physical and chemical properties often depend on the atomic structure of the interface between oxide and metal, which is in turn driven by the low coordination of atoms, the nature of bonds at the interface, as well as related elastic and polarity-driven effects.[7,8] In addition, the structural and electronic properties of thin films are determined by charge transfers at the interface, changes in the metal work function upon oxide deposition,[9−11] and, specifically for transition metal oxides, the possibility of having cations in different oxidation states.[12] The synergy of all these effects gives rise to very complex phase diagrams of low-dimensional oxide structures supported on metals (see ref 13 and references therein).

The ultrathin films consisting of just a single layer of oxide often show structural and electronic properties different from their bulk counterparts. The limited thickness has also a strong impact on the properties of metal clusters deposited onto these films. For example, while remaining neutral on thicker films, Au atoms may be positively or negatively charged when supported on ultrathin oxide films.[14−18] Therefore, for these systems, the thickness of the oxide film and the nature of the metal substrate play the decisive role. Very recently, it has been demonstrated that the film thickness matters not only for metal particles but also for gas phase molecules reacting at the surface.[19,20] Indeed, bilayer FeO(111) films supported on Pt(111) have been shown to be much more active in low temperature CO oxidation than Pt(111).[21,22] The proposed mechanism involves, prior to the reaction with CO, the transformation of

the bilayer Fe−O film into a trilayer O−Fe−O (FeO_2) film, that further catalyzes CO oxidation via a Mars−van Krevelen type mechanism.[21] Theoretical modeling[22] corroborated this scenario and suggested that the oxidation of the FeO film proceeds through activation of molecular oxygen by electrons that are transferred from the oxide/metal interface, thus resulting in O_2^{2-} species, which ultimately dissociate to form an O−Fe−O film.

In the present study we aim at a deeper understanding of the oxidation of the FeO(111) film as a function of oxygen pressure and at a determination of the atomic structure of catalytically active O-rich films using density functional theory (DFT) and scanning tunneling microscopy (STM). The DFT results show that conditions under which the bilayer transforms into the trilayer film strongly depend on the region within the Moiré unit cell of the FeO(111)/Pt(111) film where oxidation takes place. The site specificity of the oxidation process can explain the experimentally observed formation of an ordered pattern of FeO_{2-x} islands rather than of a continuous FeO_2 film. Moreover, a high resolution STM study revealed a $(\sqrt{3} \times \sqrt{3})R30°$ superstructure of FeO_{2-x} islands with respect to the pristine FeO film. This structure was rationalized by DFT in terms of buckling effects in the Fe sublayer and may be considered as an intermediate state toward the formation of an iron[23] or ferryl (Fe=O)[24] terminated $Fe_2O_3(0001)$ film at elevated oxygen pressures.

2. Methods and Materials

The experiments were carried out in an ultrahigh vacuum (UHV) chamber equipped with low energy electron diffraction/ Auger electron spectroscopy (LEED/AES), quadrupole mass-spectrometer, and STM. The preparation of the FeO(111) films includes vapor deposition of $\sim 1 \times 10^{15}$ at/cm^2 of Fe onto clean Pt(111) at 300 K and subsequent annealing in 10^{-6} mbar O_2 at 1000 K for 2 min. The temperature was measured by a chromel−alumel thermocouple spot-welded to the edge of the Pt(111) crystal, which is in turn clamped to the Pt sample holder.

* Corresponding authors. E-mail: livia.giordano@mater.unimib.it (L.G.); shaikhutdinov@fhi-berlin.mpg.de (S.S.).
† Università di Milano-Bicocca.
‡ Fritz-Haber-Institut.
§ CNRS, Institut des Nanosciences de Paris.
∥ UPMC Université Paris 06.

Transformations of an FeO(111) Film on Pt(111)

J. Phys. Chem. C, Vol. 114, No. 49, 2010 **21505**

For high pressure oxidation, the sample was transferred into the small (~1*l*) cell pressurized to 20 mbar of O_2 (99.999%) that was additionally cleaned using a cold trap kept at ~150 K.

The computational setup is similar to the one used in our earlier studies of the FeO/Pt(111) system.[25,17] We use the DFT + U approach to correct the inherent limitations of the method in describing late transition metal oxides with localized states. We adopt the approach of Dudarev et al.,[26] with $U_{Fe} - J_{Fe} = 3$ eV, as implemented in the VASP code.[27,28] The present approach satisfactorily reproduces the properties of bulk FeO and Fe_2O_3, involving iron in formal Fe^{2+} and Fe^{3+} oxidation states, respectively. The calculations have been performed within the generalized gradient approximation using the Perdew–Wang 91 (PW91) functional,[29] a plane wave basis set with kinetic energy cut off of 400 eV, and the projector augmented wave method.[30,31]

Due to the mismatch with the Pt substrate the FeO oxide bilayer forms a Moiré superstructure with a large periodicity (about 26 Å).[32–34] The three qualitatively different regions of the Moiré unit cell in the FeO/Pt(111) and FeO_2/Pt(111) systems can be classified by the local registry of the Fe ions and the Pt(111) substrate. In the "Fe-fcc" region both Fe and interface O atoms are in 3-fold hollow positions with respect to the Pt(111) substrate. In the "Fe-hcp" region the O atoms in contact with the metal surface are on top of a surface Pt atom, while the Fe atoms adsorb in the hollow position. Finally, in the "Fe-top" region the interface O atoms are in the hollow positions and the Fe atoms are on top of a surface Pt.

In the present study we use two qualitatively different interface models, which have already been employed and described in detail in our previous works.[18,25] For thermodynamic calculations we use a (2 × 2)-FeO(111) on (2 × 2)-Pt(111) pseudomorphic configuration for each of the high symmetry regions of the periodic Moiré cell: Fe-top, Fe-fcc, and Fe-hcp. Each of these regions is thus described separately by a specific unit cell, where the lattices are aligned and the Pt(111) substrate is expanded in order to match the oxide in-plane lattice parameter (a = 3.10 Å). Used in the past,[25,35,36] such a pseudomorphic model provides a local description of the substrate work function consistent with that obtained from most recent calculations including the full Moiré cell.[40] Using the (2 × 2) model we considered FeO_x phases with x = 0.75, 1.00, 1.25, 1.50, 1.75, 2.00, and 2.25 by varying the number of oxygen atoms in the unit cell. The magnetic ordering in the considered iron oxides corresponds to a row-wise antiferromagnetic structure, RW-AF-(2 × 1), used previously in studies on FeO(111)/Pt(111).[25]

In order to account for the experimental ($\sqrt{3} \times \sqrt{3}$)R30° oxygen-rich structure we employ also a nonpseudomorphic interface model, obtained by the superposition of ($\sqrt{3} \times \sqrt{3}$)R30°-FeO(111) and (2 × 2)-Pt(111) structures. This model requires only a small (3%) distortion of the Pt(111) substrate to provide the matching between the two lattices at the experimental value of FeO(111) lattice parameters, and has been already successfully used for single atom adsorption onto FeO(111)/Pt(111).[18] In the nonpseudomorphic model, similarly to the real structure, the two lattices are not aligned and the three high symmetry regions (sites) are located along the cell diagonal. The considered magnetic ordering is antiferrimagnetic with $2/3$ of cations with the same magnetization and $1/3$ with opposite magnetization.

In the above models, the Pt(111) substrate is represented by five atomic layers and the oxide film is placed on one side of the metal slab. The slabs are separated by at least 10 Å of

vacuum, and so-called dipole corrections are applied in order to eliminate the residual dipoles in the direction perpendicular to the surface. In the pseudomorphic model, in order to mimic the structural constraint of the Moiré superstructure, for the three configurations (Fe-top, Fe-hcp, Fe-fcc) the registry between the FeO and Pt lattices is maintained by fixing the lateral position of two out of four interface ions (oxygen for Fe-hcp registry; iron for Fe-top and Fe-fcc registry). Within this model all other coordinates of the oxide films and the vertical coordinates of the Pt atoms are allowed to relax. While necessarily approximate, such an approach maintains the local registry in the Moiré cell and enables a separate treatment of each of the three different regions. In the nonpseudomorphic model, all coordinates of the oxide and the vertical coordinates of the metal substrate are optimized. The atomic coordinates are relaxed until the residual forces become smaller than 0.01 eV/Å. The Brillouin zone of the pseudomorphic cell is sampled on a (5 × 5 × 1) Monkhorst–Pack grid, and a (6 × 6 × 1) grid is used for the nonpseudomorphic cell. Atomic charges are obtained within the decomposition scheme proposed by Bader.[37,38]

Different stages of oxidation of the pristine FeO/Pt(111) film are described by imposing the chemical equilibrium between the oxide film and a reservoir of O_2 molecules in the gas phase, at a given partial pressure and temperature, characterized by the chemical potential μ_O. The oxidation-induced variation of Gibbs free energy with respect to FeO/Pt(111), can be written as

$$\Delta G = G(FeO_x/Pt) - G(FeO/Pt) - y\mu_O$$

where $y = 4(x - 1)$ for the pseudomorphic interface model. Following the usual procedure in ab initio thermodynamics,[39] ΔG is approximated by the difference of the corresponding 0 K total energies $E(FeO_x/Pt) - E(FeO/Pt)$ and of the chemical potential of gas phase oxygen containing the rotational and translational contributions only. As a reference, we choose the total energy of oxygen in an isolated oxygen molecule, namely $\mu_O(0 K, p) = 1/2E(O_2) = 0$. The oxygen chemical potential can be related to the partial pressure p and the temperature T of the oxygen gas by the expression

$$\mu_O(T, p) = \mu_O(T, p^0) + \frac{1}{2}k_B T \ln(p/p^0)$$

where $\mu_O(T, p^0)$ gives the tabulated temperature dependence at the pressure $p^0 = 1$ atm.[39] The range of oxygen chemical potentials corresponding to realistic experimental conditions has been estimated as follows. The O-rich limit, approximated conventionally by equilibrium with molecular oxygen, corresponds in our case to $\mu_O \sim 0$ eV. The O-poor limit, where oxygen progressively leaves the oxide film and iron particles are formed, is approximated by equilibrium between FeO film and bulk iron, which corresponds in our case to $\mu_O \sim -3$ eV.

3. Results and Discussion

3.1. Experimental Results. Figure 1a,b shows 150 nm × 150 nm STM images of a FeO(111)/Pt(111) film before and after exposure to 20 mbar of O_2 at 470 K for 10 min. It is clear that the oxidized surface (hereafter referred to as FeO_{2-x}) exhibits the long-range periodicity very similar to that of FeO. This is also evident from the comparison of LEED patterns shown in the insets. However, in contrast to the pristine FeO films, where
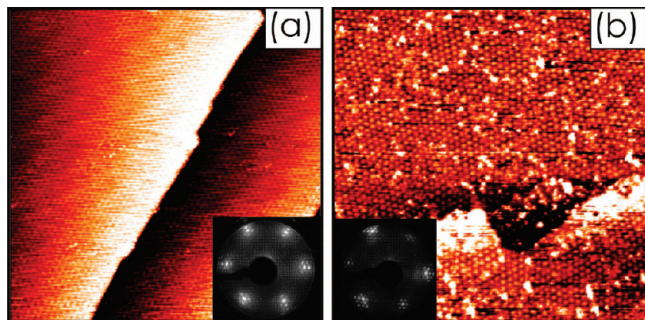
Figure 1. STM images of the FeO film before (a) and after (b) exposure to 20 mbar of O_2 at 470 K for 10 min. Image size 150 nm ×150 nm, tunneling bias and current are 0.5 V and 0.7 nA (a), and 1 V and 0.7 nA (b), respectively. The insets show the corresponding LEED patterns at 60 eV. Randomly dispersed bright protrusions on these images are assigned to contaminations (primarily, carbon as judged by AES).

the Moiré superstructure is extremely well ordered, the oxidized surface shows a multidomain structure within the same terrace.

STM images of the samples oxidized at 300 K, where both pristine and reconstructed surfaces coexist,[22] reveal that the Moiré lattice on the oxidized FeO_{2-x} patches is expanded by ~3%, as compared to the FeO film. (On the fully oxidized surfaces formed at ~450 K the expansion, as measured by STM, is apparently larger (up to 10%), although the uncertainty is higher, too.) Here, we have to recall that the Moiré pattern of FeO(111)/Pt(111) arises from the lattice mismatch between FeO(111) (a_{FeO} ~ 3.1 Å) and Pt(111) (a_{Pt} = 2.77 Å). Depending on the preparation, different coincidence structures have been observed using SPA (spot-profile analysis) LEED, such as $(\sqrt{84} \times \sqrt{84})R10.9°$ and $(\sqrt{91} \times \sqrt{91})R5.2°$.[34] In general, there is an inverse relation between the lattice constants of the oxide layer and the Moiré superstructure: The smaller the lattice constant of FeO(111), the larger the Moiré cell, and vice versa. Therefore, the STM results suggest that the lattice constant of the FeO_{2-x} film is slightly shorter than that of FeO(111). In order to verify this finding, we performed a comparative analysis of the LEED patterns where Pt and FeO diffraction spots are clearly distinguished. The analysis reveals that the lattice constant of the oxide film, indeed, decreases from 3.09 to 3.05 Å (or by ~1.5%), on average, upon high-pressure oxidation. To accommodate these small changes while maintaining a coincidence superstructure, the transformation of the FeO film into the FeO_{2-x} film must be accompanied by a small rotation with respect to the Pt(111) substrate, which is difficult to determine precisely with the conventional LEED apparatus used in our experiments. Nevertheless, these results can explain the multidomain morphology of the oxidized films, which apparently consists of domains rotated in a slightly different way (see Figure 1b).

The large scale STM images also reveal a considerably higher corrugation amplitude of the FeO_{2-x} films (~0.6 Å) as compared to the pristine FeO films (~0.1 Å), both measured at low bias voltages. Tentatively, we propose that this effect may be assigned to the formation of well-ordered, planar O−Fe−O islands, rather than of a continuous FeO_2 film, or to a wavelike buckling (rumpling) of the Fe and O sublayers, or both. High-resolution STM images revealed even more structural complexity of the oxidized films (see Figure 2). It has turned out that the FeO_{2-x} island surfaces exhibit a $(\sqrt{3} \times \sqrt{3})R30°$ structure with respect to the pristine FeO(111) more clearly seen in Figure 2b.

To explain the observed STM contrast, one could, in principle, address the stoichiometry of the oxidized film. In order to create the $(\sqrt{3} \times \sqrt{})R30°$ structure within the ideal FeO_2 film proposed
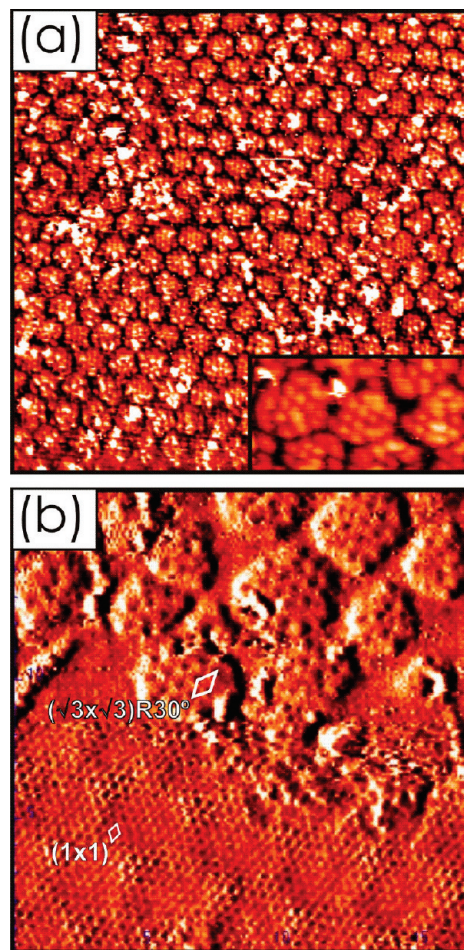

Figure 2. (a) 50 nm ×50 nm STM image of the FeO film exposed to 14 mbar of O_2 at 450 K for 10 min. The inset zooms in the $(\sqrt{3} \times \sqrt{3})R30°$ structure with respect to pristine FeO, which is more clearly observed in the image in part b, presented in the differentiated contrast, where both structures are resolved on the sample oxidized in 0.5 mbar for 10 min at 350 K. The unit cells are indicated. Tunneling bias and current are 0.25 V, 0.7 nA (a); 1.0 V, 0.7 nA (b); 0.1 V, 0.7 nA (inset), respectively.

in the model, one could remove $1/3$ or $2/3$ of the O atoms in the topmost close-packed O-layer. (Note that the amount of Fe does not change during oxidation.) This model would result in $FeO_{1.66}$ and $FeO_{1.33}$ stoichiometry, respectively. However, a thermal desorption spectroscopy (TDS) study[22] revealed two O_2 desorption peaks (one at ~840 K and another at ~1170 K, the latter was virtually identical to the peak from pristine FeO) with a (0.8−0.9):1 ratio. This implies an $FeO_{1.8}$ stoichiometry which is in good agreement with Auger spectroscopy data. Therefore, the TDS and AES results are inconsistent with models suggesting an oxygen deficiency in the topmost O-layer. The fact that the experimentally observed stoichiometry of the oxidized films is not exactly FeO_2 could be explained by an incomplete transformation of the film as observed by STM.

In addition, we find that the observation of the $(\sqrt{3} \times \sqrt{3})R30°$ structure by STM is not limited to the particular tunneling conditions and bias polarity. This favors the conclusion that the STM contrast is determined by Fe rather than O species forming electronic states near the Fermi level. Therefore, the combined STM, TDS, and AES results suggest a buckling of the Fe layer upon oxidation.

3.2. Ab Initio Oxidation Thermodynamics of the FeO/Pt(111) Film. While the structural characteristics and the interaction with atomic hydrogen have been recently treated
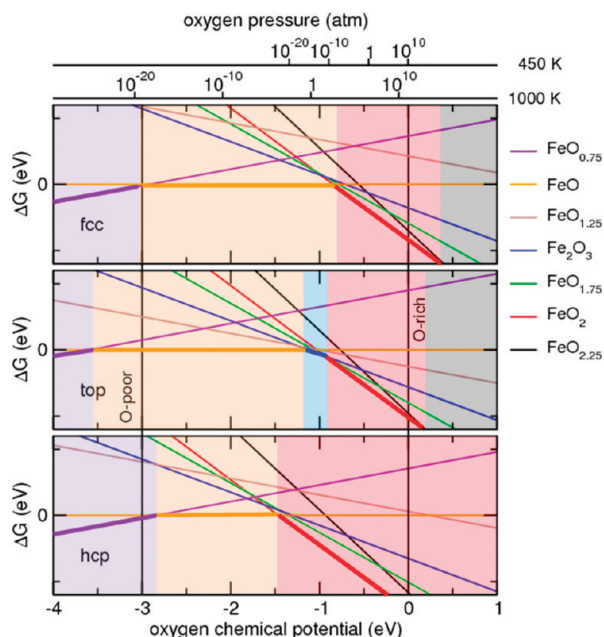
Figure 3. Oxidation-induced change of Gibbs free energy ΔG (eV) of the FeO/Pt(111) film as a function of oxygen chemical potential (eV), for the three high-symmetry regions of the Moiré cell. Each line represents the most stable structure for a given stoichiometry. The bold lines and the background colors represent the most stable structure for a given oxygen chemical potential.

explicitly using the full Moiré cell,[40,41] the size of the FeO(111)/Pt(111) Moiré pattern (about 26 Å) renders its direct use for ab initio thermodynamic calculations computationally prohibitive. To circumvent this difficulty, we perform separately the analysis of oxide phases in different regions of the Moiré pattern and link the results by the common reference to oxidation conditions (value of oxygen pressure), in order to construct a complete region-dependent phase diagram. This approach allows us to unravel the general physical mechanisms related to the structural transformation and in particular the site-dependent stabilization of the FeO$_2$ phase.

The phase diagrams for a FeO$_x$ film in the three high symmetry regions of the Moiré pattern as a function of the oxygen chemical potential are shown in Figure 3. While several alternative configurations for each oxide stoichiometry x have been considered and optimized, only the most stable one for each x is plotted.

As expected, the increase of oxygen partial pressure induces a progressive stabilization of the phases with higher oxygen content. Due to the considerable vacancy formation energy, only in extremely oxygen-poor conditions, $\mu_O < -3.0$ eV, oxygen vacancies (violet line in Figure 3) appear in the FeO(111) film, in agreement with the experimental findings.[22]

The FeO film (orange line in Figure 3) is stable in a relatively large range of oxygen chemical potentials, but the stability window is quite sensitive to the region of the Moiré pattern. Indeed, it extends up to $\mu_O = -0.8$ eV, -1.1 eV, and -1.5 eV, respectively, in the Fe-fcc, Fe-top, and Fe-hcp regions. Moreover, while in Fe-hcp and Fe-fcc the incorporation of oxygen into the pristine film stabilizes directly the oxygen-rich phase of FeO$_2$ stoichiometry (red line in Figure 3), in the Fe-top region it involves a stable intermediate phase of Fe$_2$O$_3$ stoichiometry (blue line in Figure 3), for -1.1 eV $< \mu_O < -0.9$ eV. Let us note that the precise stoichiometry of this phase may be partially biased by the use of the (2 × 2) model. Indeed, analogous calculations in the nonpseudomorphic ($\sqrt{3} \times \sqrt{3}$)R30° model

provide evidence for an intermediate phase of an Fe$_3$O$_4$ stoichiometry.

Regardless of the region of the Moiré pattern, the FeO$_2$ film has a trilayer structure with the three atomic layers in fcc stacking. While detailed structural and electronic characteristics of this phase will be discussed in the next section, let us point out that its enhanced stability in the Fe-hcp region is driven principally by short covalent Pt−O bonds, enabled by the preferential O on top of Pt geometry.

Finally, in all cases, adsorption of an additional oxygen atom on the FeO$_2$ film requires extremely oxygen-rich conditions ($\mu_O > 0.5$ eV, not shown), where it competes with the condensation of molecular oxygen on the surface. We note that two qualitatively different configurations are in competition for atomic oxygen adsorption. Either a ferryl (Fe=O) group is formed, causing a strong outward relaxation of the Fe atom, or a peroxo group is formed involving one oxygen atom in the surface layer of FeO$_2$. Their relative stability depends on the region in the Moiré.

The above results clearly show that under given conditions several oxide phases of different structure and stoichiometry may compete and/or coexist within the Moiré pattern. In particular, at low oxygen pressure ($\mu_O \sim -1.3$ eV) one expects an ordered array of FeO$_2$ islands, limited to the Fe-hcp regions of the FeO(111)/Pt(111) template. At somewhat higher oxygen pressure ($\mu_O \sim -1.0$ eV), these islands shall coexist with an intermediate oxide phase in the Fe-top regions of the Moiré pattern. Finally, beyond $\mu_O \sim -1.0$ eV, one expects the FeO$_2$ trilayer to cover the entire Pt(111) surface. The experimental situation is of course much more complex, even if all kinetic considerations are put aside. Indeed, one may expect a progressive oxidation-driven change of local in-plane lattice parameters in the oxide layer, direct and substrate-mediated interactions between the different regions of the oxidizing pattern, and/or constraints due to finite sizes of the oxide structures. Additionally, structures present at different stages of the oxidation process may tend to change their local registry with the substrate in order to optimize the interface energy. This latter effect is clearly suggested by the strong preference for the on top Pt position of interfacial oxygen ions at the FeO$_2$(111)/Pt(111) interface.

3.3. Ab Initio Characterization of the FeO$_2$/Pt(111) Film. We now address the experimental results associated with the oxygen-rich islands, for which both the experimental (section 3.1) and the theoretical (section 3.2) results point toward formation of a trilayer structure with a formal FeO$_2$ stoichiometry at the oxygen pressures and temperatures used in the experiments. In order to rationalize the experimentally observed ($\sqrt{3} \times \sqrt{3}$)R30° structure of the oxygen-rich islands, we adopt the nonpseudomorphic interface model with a ($\sqrt{3} \times \sqrt{3}$)R30°−FeO(111)//(2 × 2)-Pt(111) unit cell. Structural optimization shows that this coincidence cell enables all interfacial oxygen of the FeO$_2$ trilayer to form a single short Pt−O bond, which is consistent with the stabilizing mechanism identified above.

Beyond this general feature, a careful structural optimization reveals the existence of two quasidegenerate structures of the FeO$_2$ trilayer as shown in Figure 4 (hereafter referred to as "planar" and "buckled" structures). The small energy difference obtained from 0 K calculations (less than 0.04 eV/FeO$_2$) may be hardly sufficient for a valid estimation of the actual stability under experimental conditions. Since additionally the energetics is very sensitive to the precise value of the in-plane lattice parameter and to the choice of U parameter in the DFT + U approach, in the following we present and discuss both structures.
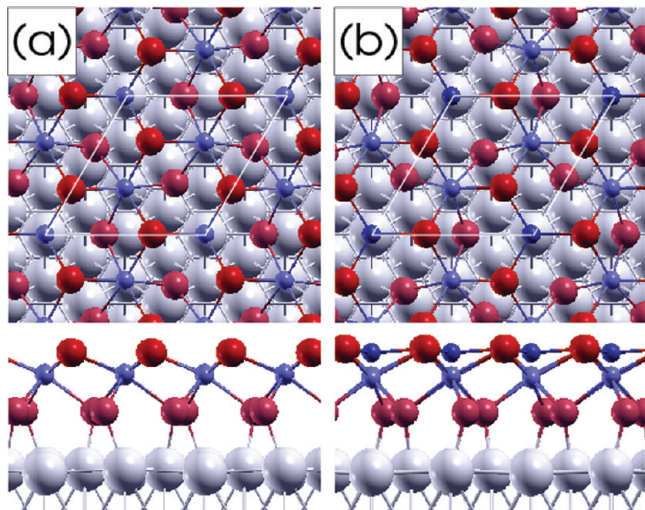
Figure 4. Top and lateral views of the two quasidegenerated structures of the FeO$_2$ trilayer: planar (a) and buckled (b). Platinum atoms are displayed as large (gray) spheres, oxygen atoms as intermediate size (red) spheres, and iron atoms as small (blue) spheres. Darker spheres represent oxygen and iron atoms in the topmost layer.

The "planar" FeO$_2$ trilayer is only slightly distorted with respect to the (2×2) structure obtained with the pseudomorphic model. All Fe cations are 6-fold coordinated and are located at a similar distance from the Pt(111) surface, forming a nearly flat Fe sublayer (the intralayer corrugation is less than 0.08 Å) (see Figure 4). All anions in the oxide have three Fe neighbors. The film is asymmetric: The average Fe−O interlayer distance at the interface side (1.23 Å) is almost twice that at the surface (0.75 Å). The charge analysis provides evidence for a formal Fe^{3+} oxidation state of all iron ions and an electron transfer from the metal substrate, which enables a formal O^{2-} valence of surface and interface oxygens.[8,22]

Although the dipole moment due to the asymmetry of the planar FeO$_2$ film considerably attenuates the effect, the electron transfer toward the oxide film enhances substantially (by 2.0 eV) the work function of planar FeO$_2$/Pt with respect to a bare Pt(111) surface. At variance, in the FeO(111)/Pt(111) system, the large electronegativity of Pt drives the electrons toward the metal, and provokes an outward relaxation of the O layer, compensating the dipole moment due to the electron transfer.[11,18] In this case, the small reduction of the work function with respect to the bare Pt(111) surface (-0.3 eV) is driven primarily by the compression of the electron density at the interface. The local density of states (LDOS) of the supported FeO$_2$ film, shown in Figure 5, reveals a small separation between the top of the valence band of mixed Fe−O character and the bottom of the conduction band of essentially Fe 3d character (full, dashed, and dashed−dotted black lines in Figure 5). Antibonding states due to the covalent O−Pt bond at the interface can be seen in the LDOS of interfacial oxygen (full red line in Figure 5), in this low density region.

The "buckled" FeO$_2$ film undergoes a substantial local distortion. Two out of three cations in the unit cell remain 6-fold coordinated, but the third Fe ion flips outward almost at the height of the topmost oxygen layer (Figure 4). The resulting corrugation of the Fe atomic layer is large (0.87 Å), and the surface of the FeO$_2$ film consists of a nearly flat structure of 3-fold coordinated Fe and O ions with a well pronounced $(\sqrt{3} \times \sqrt{3})R30°$ symmetry. All anions at the interface with Pt have two Fe neighbors only. Our results show that such a structural distortion is not associated with a substantial change
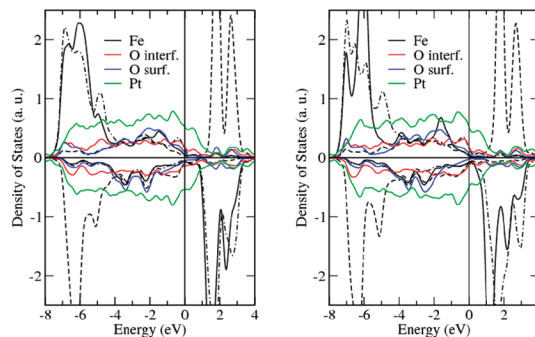

Figure 5. Densities of states of the two quasidegenerated structures of the FeO$_2$ trilayer: planar (left) and buckled (right). The three black lines (solid, dashed, and dashed−dotted) represent the projection on the three inequivalent iron atoms in the unit cell. For the buckled structure, full black line corresponds to the 3-fold coordinated Fe.
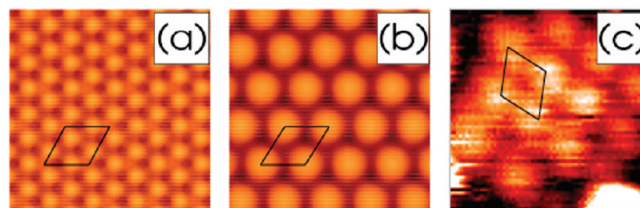

Figure 6. Simulated STM images for the two quasidegenerated structures of the FeO$_2$ trilayer: planar (a) and buckled (b). Image size = 25 Å × 25 Å, V_{bias} = 1.0 V, and electron charge isodensity = 1 × 10^{-5} e/Å^3. Experimental STM image (c) showing the $(\sqrt{3} \times \sqrt{3})R30°$ structure of an oxygen-rich island. Size 25 Å × 25 Å, bias 1 V, and current 0.7 nA.

of the electronic structure. In particular, the electron transfer at the interface and the oxidation state of all ions remain practically unaltered. We note that the outward buckling of the Fe sublayer enhances the asymmetry of the oxide film (separation between centers of gravity of positive and negative charges) and thus opposes the dipole moment due to the electron transfer toward the oxide film. As a consequence the work function of a buckled FeO$_2$/Pt film is only 1.1 eV larger than that of the bare Pt(111) surface. In analogy to the adsorbate-induced rumpling inversion found in Pt-supported FeO(111) films,[18] we note that a similar buckling effect can be induced by adsorbates.

The structural buckling modifies the Fe-projected density of states (see Figure 5). The LDOS of the 3-fold coordinated cations (full black line in Figure 5) is considerably narrowed (majority valence d states) and shifted toward lower energies (minority conduction d states) with respect to the 6-fold coordinated ones (black dashed and dashed−dotted lines in Figure 5). This latter effect results in a small downward shift of the bottom of the conduction band of the FeO$_2$ film.

Isodensity plots of electronic states in the [0, 1] V energy window, shown in Figure 6, are used to simulate STM images taken in the constant current mode at a bias of 1 V. Our results suggest that, at this bias, the STM images are dominated by ions in the topmost layer: surface oxygens in the case of planar film structure and both surface oxygens and the flipped Fe ion in the case of buckled film structure. In particular, the contribution of Fe ions is substantially different in the two structures. While in the planar structure Fe ions contribute only a little to the STM contrast, the 3-fold coordinated Fe atoms of the buckled structure are clearly visible and dominate the STM image at all biases (not shown). As a consequence, three spots per $(\sqrt{3} \times \sqrt{3})R30°$ unit cell are visible for the planar structure, while only one spot appears for the buckled one. Bearing in mind that STM images may depend on the precise tip configuration during the experiments, the simulated images are in fair

Transformations of an FeO(111) Film on Pt(111)

J. Phys. Chem. C, Vol. 114, No. 49, 2010 **21509**

agreement with the STM results (see Figure 2a) suggesting that the buckled surface may explain the experimentally observed $(\sqrt{3} \times \sqrt{3})R30°$ structure.

Interestingly, the buckled film, with all the iron atoms in the formal Fe^{3+} oxidation state, approaches the structure of the Fe-terminated $Fe_2O_3(0001)$ hematite. It is well-known that the formation of bulk Fe_2O_3 is thermodynamically favorable at high oxygen pressures. The surface termination of $Fe_2O_3(0001)$ depends on the oxygen partial pressure[23] and may, under certain conditions, be ferryl (Fe=O) terminated.[24] The preliminary infrared spectroscopy results did not reveal either Fe or Fe=O surface species in our samples studied at relatively low oxidation temperatures (~450 K). Therefore, we can consider the $(\sqrt{3} \times \sqrt{3})R30°$ structure as an intermediate state in the transformation of the FeO(111) into the $Fe_2O_3(0001)$ film.

4. Conclusions

The oxidation of the FeO(111) film as a function of oxygen pressure was studied using STM and DFT. The DFT results show that conditions under which the bilayer FeO film transforms into the trilayer FeO_2 film depend strongly on the region within the coincidence (Moiré) unit cell of FeO(111)/Pt(111). The results allow us to sketch a quite general mechanism, revealing a progressive oxidation of a patterned oxide film, where strongly region-dependent stability of oxide phases may lead to different iron oxidation states in different regions of the film, and, thus, to the formation of ordered oxide structures with different stoichiometries. Indeed, the strong site specificity of the FeO(111) oxidation process explains the experimentally observed formation of an ordered pattern of FeO_2 islands. Moreover, a high resolution STM study reveals a $(\sqrt{3} \times \sqrt{3})R30°$ superstructure of the FeO_2 islands with respect to the pristine FeO film. This structure was rationalized by DFT in terms of the preferred O on top of Pt interface registry associated with a buckling effect in the Fe sublayer. This buckled structure, where one out of three Fe atoms flips outward at the height of the topmost oxygen layer, may be considered as an intermediate state in the transformation of the FeO(111) into $Fe_2O_3(0001)$ film.

References and Notes

(1) Chambers, S. A.; Droubay, T. C.; Wang, C. M.; Rosso, K. N.; Heald, S. M.; Schwartz, D. A.; Kittilsveld, K. R.; Gamelin, D. R. *Mater. Today* **2006**, *9*, 28.
(2) Parkin, S. S. P.; Kaiser, C.; Panchula, A.; Rice, P. M.; Hughes, B.; Samant, M.; Yang, S.-H. *Nat. Mater.* **2004**, *3*, 862.
(3) Motoyama, Y.; Matsuzaki, H.; Murakami, H. *IEEE Trans. Electron Devices* **2001**, *48*, 1568.
(4) Freund, H- J.; Pacchioni, G. *Chem. Soc. Rev.* **2008**, *37*, 2224.
(5) Weber, L. F. *IEEE Trans. Plasma Science* **2006**, *34*, 268.
(6) Matulevich, Y. T.; Vink, T. J.; Zeijlmans van Emmichoven, P. A. *Phys. Rev. Lett.* **2002**, *89*, 167601.
(7) Nilius, N. *Surf. Sci. Rep.* **2009**, *64*, 595.
(8) Goniakowski, J.; Giordano, L.; Noguera, C. *Phys. Rev. B* **2010**, *81*, 205404.
(9) Giordano, L.; Cinquini, F.; Pacchioni, G. *Phys. Rev. B* **2006**, *73*, 045414.
(10) Prada, S.; Martinez, U.; Pacchioni, G. *Phys. Rev. B* **2008**, *78*, 235423.
(11) Goniakowski, J.; Noguera, C. *Phys. Rev. B* **2009**, *79*, 155433.
(12) Netzer, F. P.; Allegretti, F.; Surnev, S. *J. Vac. Sci. Technol., B* **2010**, *28*, 1.
(13) Netzer, F. P. *Surf. Sci.* **2010**, *604*, 485.
(14) Pacchioni, G.; Giordano, L.; Baistrocchi, M. *Phys. Rev. Lett.* **2005**, *94*, 226104.
(15) Sterrer, M.; Risse, T.; Martinez Pozzoni, U.; Giordano, L.; Heyde, M.; Rust, H.-P.; Pacchioni, G.; Freund, H.-J. *Phys. Rev. Lett.* **2007**, *98*, 096107.
(16) Frondelius, P.; Hellman, A.; Honkala, K.; Häkkinen, H.; Grönbeck, H. *Phys. Rev. B* **2008**, *78*, 085426.
(17) Giordano, L.; Pacchioni, G.; Goniakowski, J.; Nilius, N.; Rienks, E. D. L.; Freund, H.-J. *Phys. Rev. Lett.* **2008**, *101*, 026102.
(18) Goniakowski, J.; Noguera, C.; Giordano, L.; Pacchioni, G. *Phys. Rev. B* **2009**, *80*, 125403.
(19) Grönbeck, H. *J. Phys. Chem. B* **2006**, *110*, 11977.
(20) Hellman, A.; Klacar, S.; Grönbeck, H. *J. Am. Chem. Soc.* **2009**, *131*, 16636.
(21) Sun, Y.-N.; Qin, Z.-H.; Lewandowski, M.; Carrasco, E.; Sterrer, M.; Shaikhutdinov, S.; Freund, H.-J. *J. Catal.* **2009**, *266*, 359.
(22) Sun, Y.-N.; Giordano, L.; Goniakowski, J.; Lewandowski, M.; Qin, Z.-H.; Noguera, C.; Shaikhutdinov, S.; Pacchioni, G.; Freund, H.-J. *Angew. Chem., Int. Ed.* **2010**, *49*, 1.
(23) Shaikhutdinov, S.; Weiss, W. *Surf. Sci.* **1999**, *432*, L627.
(24) Lemire, C.; Bertarione, S.; Zecchina, A.; Scarano, D.; Chaka, A.; Shaikhutdinov, S.; Freund, H.-J. *Phys. Rev. Lett.* **2005**, *94*, 166101.
(25) Giordano, L.; Pacchioni, G.; Goniakowski, J.; Nilius, N.; Rienks, E. D. L.; Freund, H.-J. *Phys. Rev. B* **2007**, *76*, 075416.
(26) Dudarev, S. L.; Botton, G. A.; Savrasov, S. Y.; Humphreys, C. J.; Sutton, A. P. *Phys. Rev. B* **1998**, *57*, 1505.
(27) Kresse, G.; Hafner, J. *Phys. Rev. B* **1993**, *47*, R558.
(28) Kresse, G.; Furthmüller, J. *Phys. Rev. B* **1996**, *54*, 11169.
(29) Perdew, J. P.; Chevary, J. A.; Vosko, S. H.; Jackson, K. A.; Pederson, M. R.; Singh, D. J.; Fiolhais, C. *Phys. Rev. B* **1992**, *46*, 6671.
(30) Blöchl, P. E. *Phys Rev. B* **1994**, *50*, 17953.
(31) Bengone, O.; Alouani, M.; Blöchl, P. E.; Hugel, J. *Phys Rev. B* **2000**, *62*, 16392.
(32) Vurens, G. H.; Salmeron, M.; Somorjai, G. A. *Surf. Sci.* **1988**, *201*, 129.
(33) Kim, Y. J.; Westphal, C.; Ynzunza, R. X.; Galloway, H. C.; Salmeron, M.; Van Hove, M. A.; Fadley, C. S. *Phys. Rev. B* **1997**, *55*, R13448.
(34) Ritter, M.; Ranke, W.; Weiss, W. *Phys. Rev. B* **1998**, *57*, 7240.
(35) Galloway, H. G.; Sautet, P.; Salmeron, M. *Phys. Rev. B* **1996**, *54*, R11145.
(36) Merte, L. R.; Knudsen, J.; Grabow, L. C.; Vang, R. T.; Lægsgaard, E.; Mavrikakis, M.; Besenbacher, F. *Surf. Sci.* **2009**, *603*, L15.
(37) Bader, R. F. W. *Chem. Rev.* **1991**, *91*, 893.
(38) Henkelman, G.; Arnaldsson, A.; Jónsson, H. *Comput. Mater. Sci.* **2006**, *36*, 254. Tang, W.; Sanville, E.; Henkelman, G. *J. Phys.: Condens. Matter* **2009**, *21*, 084204.
(39) Reuter, K.; Scheffler, M. *Phys. Rev. B* **2001**, *65*, 035406.
(40) Zhang, W.; Li, Z.; Luo, Y.; Yang, J. *J. Phys. Chem. C* **2009**, *113*, 8302.
(41) Knudsen, J.; Merte, L. R.; Grabow, L. C.; Eichhorn, F. M.; Porsgaard, S.; Zeuthen, H.; Vang, R. T.; Lægsgaard, E.; Mavrikakis, M.; Besenbacher, F. *Surf. Sci.* **2010**, *604*, 11.